Consistency Condition and ML-EM Checkerboard Artifacts

Jiangsheng You, *Member, IEEE*, Jing Wang, and Zhengrong Liang, *Senior Member, IEEE*

***Abstract*--The expectation maximization (EM) algorithm for the maximum likelihood (ML) image reconstruction criterion generates severe checkerboard artifacts in the presence of noise. A classical remedy is to impose an *a priori* constraint for a penalized ML or maximum *a posteriori* probability solution. The penalty reduces the checkerboard artifacts and also introduces uncertainty because *a priori* information is usually unknown in clinic. Recent theoretical investigation reveals that the noise can be divided into two components. One is called null-space noise which annihilates during filtered backprojection (FBP)-type analytical image reconstruction. The other is called range-space noise which propagates into the FBP-type analytically reconstructed image. In particular, the null-space noise can be numerically estimated. The aim of this work is to investigate the relation between the null-space noise and the checkerboard artifacts in the ML-EM image reconstruction from noise projection data. It is expected that removing the null-space noise from the projection data could improve the signal-to-noise ratio of the data and, therefore, reduce the checkerboard artifacts in the ML-EM reconstructed images. The expectation was realized by computer simulation studies with application to single photon emission computed tomography, where the noise has been a major factor for image degradation. The reduction of the ML-EM checkerboard artifacts by removing the null-space noise avoids the uncertainty of using *a priori* penalty.**

I. Introduction

IMAGE reconstruction in single photon emission computed tomography (SPECT) is described mathematically by the attenuated Radon transform [1]. Inverting the transform by filtered backprojection (FBP)-type formula became feasible due to the work of Novikov [2]. Thereafter, more theoretical investigations have revealed great insights in the inversion, especially its consistency condition in the presence of noise [3]. This work aims to relate the condition to the well-known checkerboard artifacts [4] in the ML-EM (maximum-likelihood expectation-maximization) image reconstruction algorithm [5-7]. The presentation of this work is organized as follows. In section II, some basics about the attenuated Radon transform are reviewed in two dimensions for presentation simplicity. In section III, the ML-EM approach to the inversion of the attenuated Radon transform is outlined briefly. In section IV, we describe the consistency condition of the attenuated Radon transform. The relation between the consistency condition and the checkerboard artifacts is numerically demonstrated in section V, followed by discussion and conclusion in section VI.

Manuscript received October 26, 2006. This work was supported in part by the U.S. NIH under Grant No. CA082402 and CA110186.

J. You is with Cubic Imaging LLC, 264 Grove St., Auburndale, MA 02466, USA and Department of Radiology, State University of New York, Stony Brook, NY 11794, USA (e-mail: jyou@cubic-imaging.com).

J. Wang is with Departments of Radiology and Physics & Astronomy, State University of New York, Stony Brook, NY 11794, USA (e-mail: jingwang@mil.sunysb.edu).

Z. Liang is with Departments of Radiology and Computer Science, State University of New York, Stony Brook, NY 11794, USA (e-mail: jzl@mil.sunysb.edu).

II. Attenuated Radon Transform and Measurement Noise

Denote by R^2 the two-dimensional (2D) planar space with coordinate representation (x, y) in the Cartesian system and (r, φ) in the polar system, and S^1 the unit vectors represented by $\vec{\theta} = (\cos\theta, \sin\theta)$ with $\theta \in [0, 2\pi]$. Assume $f(x,y)$ is a function of R^2 and

$$f_\theta(s,t) = f(s\cos\theta - t\sin\theta, s\sin\theta + t\cos\theta) \quad (1)$$

stands for the same function in the Cartesian coordinates $(s,t)_\theta$ after rotation by an angle θ along the counterclockwise direction. The coordinates $(s,t)_\theta$ and (x, y) are related by

$$\begin{pmatrix} s \\ t \end{pmatrix} = \begin{pmatrix} \cos\theta & \sin\theta \\ -\sin\theta & \cos\theta \end{pmatrix} \begin{pmatrix} x \\ y \end{pmatrix} \quad \text{and} \quad \begin{pmatrix} x \\ y \end{pmatrix} = \begin{pmatrix} \cos\theta & -\sin\theta \\ \sin\theta & \cos\theta \end{pmatrix} \begin{pmatrix} s \\ t \end{pmatrix}. \quad (2)$$

Considering that (x, y) is defined for the static object while $(s,t)_\theta$ is associated with the rotating detector, we call (x, y) the object coordinates and $(s,t)_\theta$ the detector coordinates.

In SPECT imaging, function $f(x,y)$ represents the radiotracer concentration distribution inside the human body. Gamma photons emitted at position (x, y) inside the body are linearly attenuated by the body tissues before they arrive at location $(s,t)_\theta$ on the detector surface. Let $\mu(x, y)$ stand for the distribution of linear attenuation coefficients and $p(s,\theta)$ be the accumulated photon counts at s along the view angle θ in the coordinates $(s,t)_\theta$, then $p(s,\theta)$ is expressed as:

$$p(s,\theta) = \int_{-\infty}^{\infty} f_\theta(s,\tau) e^{-a_\theta(s,\tau)} d\tau \quad (3)$$

where $a_\theta(s,\tau) = \int_\tau^\infty \mu_\theta(s,t)dt$. Equation (3) is the so-called attenuated Radon transform of $f(x,y)$, and is denoted by $\mathbf{R}_\mu f$. Due to the limited-photon counting statistics in SPECT imaging, the projection measurements are noisy and may be denoted by

$$\tilde{p}(s,\theta) = p(s,\theta) + n(s,\theta) \tag{4}$$

where $n(s,\theta)$ represents the Poisson noise which is dependent on the projection signal $p(s,\theta)$. Because of the Poisson nature of photon counting statistics, $\tilde{p}(s,\theta)$ is usually assumed to be a Poisson-point process, see reference [8] for detailed definition and properties of Poisson-point process. Assume that attenuation map $\mu(x,y)$ is known and projection measurement $\tilde{p}(s,\theta)$ is available, then the goal of SPECT image reconstruction is to estimate $f(x,y)$ from equations (3) and (4). This topic has been investigated for several decades using a variety of different methods. Briefly, there are two typical classes of methods for the image reconstruction from projections. One class consists of analytical algorithms which are based on exact inversion formulae in continuous space, for example the algorithm of [9] if the attenuation is ignored, [10] if the attenuation is uniform and [2] if the attenuation is non-uniform, after the noise is filtered. The other class consists of iterative algorithms which model the data noise distribution as a cost function or criterion with the data mean as given by equation (3) in discrete space and then minimize the cost function for image reconstruction. The EM algorithm for the ML criterion is one of the most important iterative methods.

III. ML-EM Image Reconstruction and Checkerboard Artifacts

Let's first discuss the discrete version of (3) and (4). Denote by $\tilde{p}_{i,k} = \tilde{p}(s_i,\theta_k)$ a set of acquired projections at detector bin locations $\{s_i,\theta_k\}$ and $f_{m,n} = f(x_m,y_n)$ the discrete image array to be reconstructed. Figure 1 gives an illustrative view on the discrete image array $f_{m,n}$ and a projection ray $\tilde{p}_{i,k}$ at view angle θ_k and lateral position s_i on the detector surface. Let $c_{m,n}^{i,k}$ denote the fraction of each $f_{m,n}$ contributing to the projection $\tilde{p}_{i,k}$. Note that $c_{m,n}^{i,k}$ can be calculated given the voxel array (x_m,x_n) and the detector bin location (s_i,θ_k) and may include the attenuation and other image degradation factors such as collimator response and scattering. Then the discrete version of (3) and (4) can be expressed as:

$$\tilde{p}_{i,k} = \sum_{m,n} c_{m,n}^{i,k} f_{m,n} + n_{i,k} \tag{5}$$

where $n_{i,k} = n(s_i,\theta_k)$.

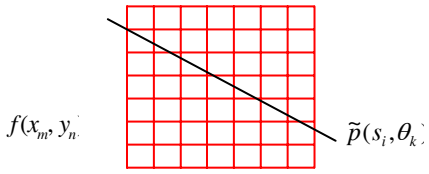

Figure 1: A discrete presentation of projection data and image array.

Obviously, one may directly solve the linear equation system (5) as the algebraic reconstruction technique (ART) does [11], assuming that the noise can be either ignored and has been filtered. By the known Poisson nature of the data noise, a statistical approach of modeling the noise property would be preferred. The well-known ML criterion is defined as:

$$L = \prod_{k,i} e^{-\sum_{m,n} c_{m,n}^{i,k} f_{m,n}} [\sum_{m,n} c_{m,n}^{i,k} f_{m,n}]^{\tilde{p}_{i,k}} \Big/ \tilde{p}_{i,k}! \,. \tag{6}$$

The goal of ML approach is to look for $f_{m,n}$ such that L arrives at the maximum for a given set of acquisition $\tilde{p}_{i,k}$. One of the most important iterative schemes for the ML image reconstruction is the EM algorithm [5]. The EM algorithm suggests the following simple iterative scheme to reach the maximum point of (6):

$$f_{m,n}^{(j+1)} = \frac{1}{\sum_{i,k} c_{m,n}^{i,k}} \sum_{i,k} c_{m,n}^{i,k} \frac{\tilde{p}_{i,k}}{\sum_{m,n} c_{m,n}^{i,k} f_{m,n}^{(j)}}, \quad j = 0, 1, \cdots . \tag{7}$$

The ML-EM reconstruction algorithm (7) generates severe checkerboard artifacts when the noise is present [4]. In order to mitigate the artifacts, Bayesian criterion was introduced in [12]. By regularization techniques such as an *a priori* constraint or a penalty function, the ML criterion (6) may be rewritten as the maximum *a posteriori* (MAP) criterion:

$$L_1 = \ln\{\prod_{k,i} e^{-\sum_{m,n} c_{m,n}^{i,k} f_{m,n}} [\sum_{m,n} c_{m,n}^{i,k} f_{m,n}]^{\tilde{p}_{i,k}} \Big/ \tilde{p}_{i,k}!\} - U[f_{m,n} - f_{m',n'}, \alpha(f)] \tag{8}$$

where $U(.)$ reflects *a priori* information and is usually expressed as a potential function on the neighborhood system, i.e., index (m',n') specifies the neighbors around (m,n) and $\alpha(f)$ may reflect any known information about the radiotracer concentration distribution [12]. By the use of the EM algorithm, an iterative MAP-EM scheme to reach the maximum point of (8) can also be derived [12]. The penalty reduces the checkerboard artifacts and also introduces uncertainty because the *a priori* information is usually unknown in clinic. In the past decades, a great effort has been devoted to investigate the noise propagation in the iterative ML-EM and MAP-EM reconstructions [13-17]. One of the main difficulties in these investigations is the high non-linearity of the ML-EM and MAP-EM algorithms. Recent theoretical investigation on FBP-type inversion of the

attenuated Radon transform reveals more insight into the noise propagation issue as shown below.

IV. FBP-type Algorithm and Consistency Condition

Since Novikov derived a FBP-type inversion formula for the attenuated Radon transform [2], a great theoretical investigation effort has been devoted to FBP-type inversion and associated noise propagation, e.g., [3]. Before introducing the Novikov's formula, we give the definition of two well-known transforms. One is the Hilbert transform which is defined as:

$$[\mathbf{H}g](s) = \frac{1}{\pi}\,\mathrm{pv}\int_{-\infty}^{\infty}\frac{g(l)}{s-l}dl\ . \tag{9}$$

The other is the Radon transform as defined by:

$$[\mathbf{R}\mu](s,\theta) = \int_{-\infty}^{\infty}\mu_\theta(s,\tau)d\tau\ . \tag{10}$$

Hereafter, we denote $\hat{s} = x\cos\theta + y\sin\theta$, $\hat{t} = y\sin\theta - x\cos\theta$ and $h(s,\theta) = [\mathbf{HR}\mu](s,\theta)$. Then, Novikov's inversion formula can be expressed as:

$$f(x,y) = \frac{1}{4\pi}\int_0^{2\pi}[\frac{\partial}{\partial s}\int_{-\infty}^{\infty}\frac{\cos(0.5[h(s,\theta)-h(l,\theta)])}{\pi(s-l)} \times \frac{e^{0.5\mathbf{R}\mu(l,\theta)+a_\theta(s,\hat{t})}}{e^{0.5\mathbf{R}\mu(s,\theta)}}\tilde{p}(l,\theta)dl\,]|_{s=\hat{s}}\,d\theta \tag{11}$$

Notice that formula (11) is slightly different from its original format in [2]. Formula (11) can be regarded as an operator, denoted by $\mathbf{N}_\mu\tilde{p}$, from functions of $R^1\times S^1$ to functions of R^2. It was proved in [18] that the FBP-type algorithms in [9, 10] can be derived as the special cases of (11).

The consistency condition for the attenuated Radon transform is to characterize when a data function $\tilde{p}(s,\theta)$ indeed can be expressed as (3) for certain object function $f(x,y)$. More detailed description of the condition can be found in [3, 19, 20], and its application to the exponential Radon transform is reported in [21-23] and to the Radon transform is reported in [24-26]. In this paper, we adapt the general expression of the condition from [3], which states that the attenuated Radon transform $p(s,\theta)$ must satisfy the following integral equation:

$$\int_0^{2\pi}[e^{0.5\mathbf{R}\mu(\hat{s},\theta)-a_\theta(\hat{s},\hat{t})}\int_{-\infty}^{\infty}\frac{\cos(0.5[h(\hat{s},\theta)-h(l,\theta)])}{\pi(\hat{s}-l)} \times e^{0.5\mathbf{R}\mu(l,\theta)}p(l,\theta)dl\,]d\theta \equiv 0 \tag{12}$$

In general, the measured projection $\tilde{p}(s,\theta)$ may not satisfy (12) due to the presence of noise, i.e., there might not exist any object function $f(x,y)$ such that $\tilde{p}(s,\theta)$ is the attenuated Radon transform of $f(x,y)$. In the following, we apply the condition to separate the noisy data into two parts. One part satisfies the condition (12) and the other part does not.

Denote $\Lambda=(-1,\ 1)$ and let B be the unit disk of R^2 and $\boldsymbol{\chi}_\mathrm{B}$ be the characteristic function of B [3]. From now on, we limit our presentation on the object function $f(x,y)$ with support in B for simplicity. For any function $g(s,\theta)$ of $\Lambda\times S^1$, it can be decomposed into the following expression:

$$g(s,\theta) = [\mathbf{R}_\mu\boldsymbol{\chi}_\mathrm{B}\mathbf{N}_\mu g](s,\theta) + \{g(s,\theta) - [\mathbf{R}_\mu\boldsymbol{\chi}_\mathrm{B}\mathbf{N}_\mu g](s,\theta)\} \tag{13}$$

where the term $[\mathbf{R}_\mu\boldsymbol{\chi}_\mathrm{B}\mathbf{N}_\mu g]$ must, from [2, 3], satisfy the condition (12). Similarly, the noise $n(s,\theta)$ can also be decomposed into $n(s,\theta) = n_R(s,\theta) + n_N(s,\theta)$, here $n_R(s,\theta)$ meets the condition (12). From the uniqueness of the attenuated Radon transform as described in [2], we can derive the following equations:

$$n_N(s,\theta) = n(s,\theta) - [\mathbf{R}_\mu\boldsymbol{\chi}_\mathrm{B}\mathbf{N}_\mu n](s,\theta) \tag{14}$$

$$[\boldsymbol{\chi}_\mathrm{B}\mathbf{N}_\mu n_N](x,y) \equiv 0 \tag{15}$$

where the component $n_N(s,\theta)$ belongs to the null space of the operator $\boldsymbol{\chi}_\mathrm{B}\mathbf{N}_\mu$, see reference [19] for more details about the null space of the Radon transform operator. Hereafter we call $n_R(s,\theta)$ the range-space noise and $n_N(s,\theta)$ the null-space noise. Equation (15) implies that the null-space noise $n_N(s,\theta)$ has no contribution at all to the image reconstruction when the FBP-type inversion algorithm (11) is used. However, the null-space noise contributes to the ML-EM image reconstruction, although it can be reduced by the *a priori* penalty via the MAP criterion. In the following, we show how the null-space noise can be estimated and how much impact of removing the null-space noise upon the ML-EM reconstruction.

V. Null-Space Noise Propagation

The null-space noise propagation was investigated through numerical simulations. We assume that the emission distribution $f(x,y)$ and attenuation map $\mu(x,y)$ are defined inside the unit disk $x^2+y^2\le 1$. Functions $f(x,y)$ and $\mu(x,y)$ are evenly sampled in $[-1,1]\times[-1,1]$ on a grid of 128×128, and $[\mathbf{R}_\mu f](s,\theta)$ is evenly sampled in $[-1,1]\times[0,2\pi]$ on a grid of 128×128. All the emission phantom, attenuation map, and reconstructed images were linearly scaled to [0, 255] for display. The attenuated noise-free projections were calculated by line integrals given the emission phantom and attenuation map. In simulating the noisy projections, the Poisson number generator in [27] was used to generate the Poisson counts assuming the noise-free projections as their corresponding mean. In measuring the difference between images $I_1(m,n)$ and $I_2(m,n)$, the L^2 norm or mean square error (MSE) was used, which has the following expression:

$$MSE(I_1,I_2) = \sqrt{\sum(I_1(m,n)-I_2(m,n))^2/(MN)} \tag{16}$$

where *M* and *N* are the image height and width, respectively. The L^2 norm of an image $I(m,n)$ is defined as:

$$L^2(I) = \sqrt{\sum I^2(m,n)/(MN)}\ . \tag{17}$$

The signal-to-noise ratio (SNR) of an estimated image $I(m,n)$ against its mean image $S(m,n)$ is defined as:

$$SNR(I,S) = L^2(I)/MSE(I,S). \quad (18)$$

A. *Phantoms and Implementation of the ML-EM algorithm*

In all numerical simulations, $f(x,y)$ was chosen as the Shepp-Logan phantom and $\mu(x,y)$ was similar to the phantom used in [18]. Their pictures are shown in Figure 2. In order to identify any artifacts that the discontinuity of the emission object and the attenuation map might have, the attenuation map was designed to have different structures compared with the Shepp-Logan emission phantom so that the discontinuous edges in the Shepp-Logan phantom and the attenuation map are different. In particular, the support region of the attenuation map is larger than the support region of the emission phantom. This is different from the phantoms used in [17].

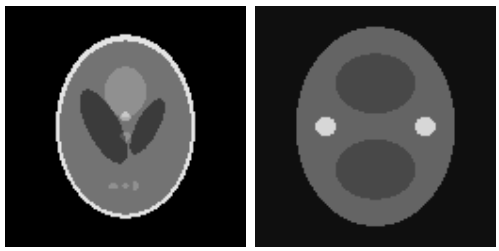

(a) (b)

Figure 2: (a) is the Shepp-Logan emission phantom and (b) is the attenuation map.

Implementation of the ML-EM algorithm (7) can be carried out through two separate steps of re-projection and back-projection. In our numerical simulations, the fast re-projector and back-projector in [28, 29] were used to realize the re-projection $\sum_{m,n} c_{m,n}^{i,k} f_{m,n}^{(j)}$ and the subsequent back-projection $\sum_{i,k} c_{m,n}^{i,k} p_{i,k}$. The rotation-based re-projector and back-projector can be described as follows. Assume that $(s_m,t_n)_{\theta_k}$ is evenly sampled for all variables. Let Δ and Ω denote the sampling interval for distance variables (x, y, s, t) and the angle variable θ, respectively. In the coordinate system $(s_m,t_n)_{\theta_k}$, the discrete re-projector becomes:

$$\tilde{p}_{i,k}^{(j)} = \sum_{m,n} c_{m,n}^{i,k} f_{m,n}^{(j)} = \Delta \sum_{n} f_{\theta_k}^{(j)}(s_i,t_n) e^{-a_{\theta_k}(s_i,t_n)} \quad (19)$$

where $a_{\theta_k}(s_i,t_n) = \Delta \sum_{j \geq n} \mu_{\theta_k}(s_i,t_j)$. The calculation of $f_{\theta_k}(s_m,t_n)$ from $f(x_m,y_n)$ is implemented through the rotation transformation of (2). The rotation is shown in Figure 3.

Similarly, in the coordinate system $(s_i,t_n)_{\theta_k}$, the back-projector along the sampling angle θ_k can be simply expressed as:

$$\frac{1}{\sum_i c_{m,n}^{i,k}} \sum_i c_{m,n}^{i,k} \frac{\tilde{p}_{i,k}}{\sum_{m,n} c_{m,n}^{i,k} f_{m,n}^{(j)}} = \frac{1}{\sum_m 1} \cdot \frac{\tilde{p}_{m,k}}{\tilde{p}_{m,k}^{(j)}}. \quad (20)$$

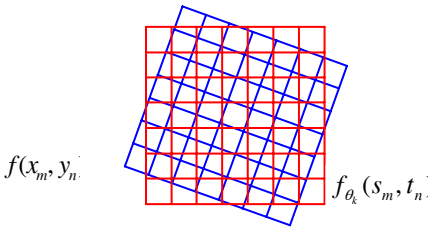

Figure 3: An illustration of image rotation.

Then through the rotation from $(s_i,t_n)_{\theta_k}$ to (x_m,y_n) and averaging all back-projections, the updated image (7) can be derived. The detailed implementation of (19)-(20) can be found in [28, 29]. By dividing the 128 projections into ordered subsets (OS) of subset size 8, the implementation becomes OS-EM image reconstruction [7].

B. *Estimate of the null-space noise and its effect upon the OS-EM reconstruction*

The Poisson counts for each detector bin were generated based on the corresponding mean projection, thus the total noise for that bin is known. In the simulation on a 128×128 array size, the total counts were 650,000 and the SNR of the noisy projection data was computed as 8.022 by equations (16)-(18). We used the numerical implementation of Novikov's inversion formula from [30] as the FBP-type algorithm without any extra filtering to realize (11). The reconstructed images from noisy projections using the FBP-type and the OS-EM algorithms are shown in Figure 4. The OS-EM algorithm was run up to 10 iterations from a uniform initial and the result of Figure 4-(b) is the best one visually after 4 iterations. The results were smoother before and diverged fast after 4 iterations, concurring with the previous studies, e.g., [4]. Both the OS-EM and FBP-type reconstructions have a similar resolution. The SNRs of the reconstructed images by the FBP-type and the OS-EM algorithms were computed as 3.60 and 2.59, respectively. It is obvious from both the SNRs and Figure 4 that the OS-EM algorithm generates noisier results than the FBP-type algorithm from the same noisy projections. The extra noise in the OS-EM reconstruction was assumed due to the null-space noise, as discussed at the end of section IV. This assumption was further validated by the study below.

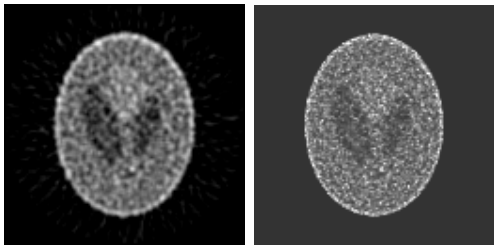

(a) (b)

Figure 4: The reconstructed images: (a) FBP-type and (b) OS-EM (4 iterations with OS size of 8) algorithms.

Next, we would use (14) to estimate the null-space noise $n_N(s_i,\theta_k)$ from the known total noise $n(s_i,\theta_k)$ in discrete

space. Theoretically, this could be done by solving the system of equations (12). Practically it is numerically challenging. For the purpose of proving the assumption made at the end of section IV, we re-projected the FBP-type reconstruction of Figure 4-(a) to estimate the noise projections without null-space noise, because the noise has annihilated in the FBP result. The re-projection was computed by line integral through the image of Figure 4-(a) and the attenuation map of Figure 2-(b). Note that the estimated $n_N(s_i,\theta_k)$ may contain numerical errors. We assume that the numerical errors can be ignored compared with the real null-space noise. Subtracting the re-projected null-space noise-free projections from the original noisy projections resulted in the null-space noise.

When the re-generated projection (which can be regarded as less noisy after the null-space noise was removed from the original noisy projection) was assumed as the mean projection, the estimated SNR of the original noisy projection is 8.021, which is very close to the true value of 8.022 above when the true mean projection was used. This closeness may suggest that $n_N(s,\theta)$ can be useful for estimating the SNR of the original noisy projections without any knowledge of the noise-free projections. Moreover, we calculated that $MSE(n,n_N)/L^2(n)=0.38$ and $MSE(n,n_R)/L^2(n)=1.02$. From these calculations, the null-space noise was clearly seen as the dominant component in the total noise using the simulated noise data above. Similar results were also observed in other noise levels and other emission phantoms and attenuation maps. Taking the simulated data at projection angle 90° as an example, the true noise and the estimated null- and range-space noises are shown in Figure 5. The close-ness of the null-space noise to the true noise is clearly seen.

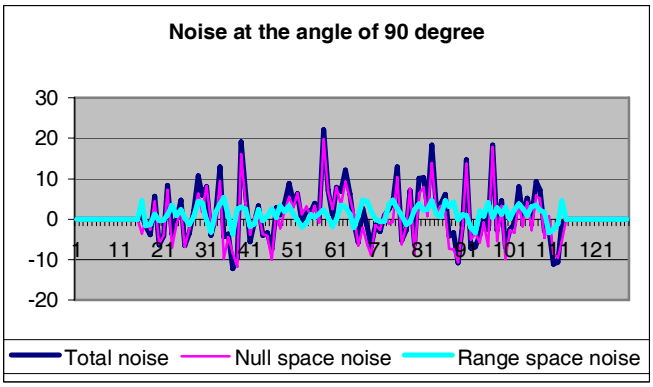

Figure 5: Illustration of the true, null space and range space noises at the angle of 90°.

After re-projecting the FBP-type reconstructed image of Figure 4-(a), the SNR of the re-generated projections was improved from 8.022 to 21.01 (after removing the null-space noise). The re-generated projections were then reconstructed respectively by the FBP-type and the OS-EM algorithms using the rotated re-projector and back-projector. The reconstructed images are shown in Figure 6. The OS-EM algorithm was run up to 20 iterations from a uniform initial and the results after 4 iterations were very similar (i.e., converged to a stable solution). This is not surprise that the re-generated projections satisfy the consistency condition. Both reconstructions are very similar visually. The SNRs of the reconstructed images changed from 3.60 to 3.71 by the FBP-type method and from 2.59 to 4.04 by the OS-EM algorithm. It can be seen that removing the null-space noise significantly improves the SNR of the projections but virtually does not change much the SNR of the reconstructed image of the FBP-type algorithm. However, it is clearly observed that the severe checkerboard artifacts in Figure 4-(b) are reduced to a large degree in Figure 6-(b) and the SNR is improved noticeably after removing the null-space noise for the OS-EM algorithm. This would suggest that the null-space noise could be a major cause of the severe checkerboard artifacts in the OS-EM or ML-EM algorithm.

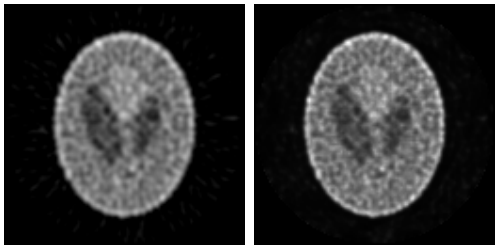

(a) (b)

Figure 6: The reconstructed images after removing the null-space noise: (a) FBP-type and (b) OS-EM (4 iterations with OS size of 8) algorithms.

VI. Discussion and Conclusion

This study investigated the well-known checkerboard artifacts of the ML-EM reconstruction algorithm by the use of the consistency condition of the attenuated Radon transform. The condition was used to separate the projection data noise into two components of null-space noise and range-space noise. The null-space noise was shown to dominate the total data noise. It was further shown that the null-space noise does not contribute to the noise propagation in the FBP-type analytical inversion reconstruction, but plays a significant role in the noise propagation in the ML-EM iterative reconstruction and is a major cause of the severe checkerboard artifacts. Removing the null-space noise stabilized the OS-EM iteration.

Characterizing and filtering the range-space noise would be a major task for FBP-type analytical reconstruction and remains an interesting research topic.

Estimating and removing the null-space noise would significantly improve the ML-EM reconstruction without *a priori* penalty. Use of the re-projection of the FBP-type result to estimate the null-space noise could be a choice, but is not very practical in computation. If a practical estimation of the null-space noise is available, a penalty for the range-space noise is still desired for ML-EM algorithm.

It was proved in [25] that forcing the projection data to be consistent with the Radon transform, by $\min\|p_N(s,\theta)\|_{L^2}$ such that $p(s,\theta) = \tilde{p}(s,\theta) + p_N(s,\theta)$ satisfies (12), does not help much for noise reduction in the inversion of the transform. This study gives an explanation that removing the null-space noise by the consistency condition does not help the noise propagation in the inversion reconstruction because the null-space noise annihilates in the inversion of the transform and the range-space noise remains. Any noise suppression must be due to the reduction of the range-space noise. The strategy of [25] could be adapted to reduce the null-space noise for OS-EM reconstruction.

Most, if not all, of previous noise reduction approaches deal with the data noise as a whole for both analytical inversion and iterative update reconstructions. This study explored an alternative strategy to separate the noise into components and deal with the components individually. Efficient means for estimation of the null-space noise is under progress. This would stabilize the OS-EM iteration so that compensation for the attenuation, scatter, collimator response and other degradation factors can be achieved under an effective control of the Poisson noise.

VII. REFERENCES

[1] Gullberg GT, The Attenuated Radon Transform: Theory and application in medicine and biology, Ph.D. Dissertation, Donner Laboratory, University of California, Berkeley, CA, 1979.

[2] Novikov RG, "An inversion formula for the attenuated X-ray transformation," *Preprint*, May of 2000, and in *Ark. Math.*, vol. 40, pp. 145-167, 2002.

[3] Novikov RG, "On the range characterization for the two-dimensional attenuated X-ray transformation," *Inverse Problems*, vol. 18, pp. 677-700, 2002.

[4] Snyder D, Miller M, Thomas L, and Politte D, "Noise and edge artifacts in ML reconstruction for emission tomography", *IEEE Trans. Medical Imaging*, vol. 6: pp. 228-238, 1987.

[5] Dempster A, Laird N, and Rubin D, "Maximum likelihood from incomplete data via the EM algorithm," *J. R. Stat. Soc. Series B*, vol. 39B, pp. 1-38, 1977.

[6] Shepp LA and Vardi Y, "Maximum likelihood reconstruction for emission tomography," *IEEE Trans. Medical Imaging*, vol. pp.113-122, 1982.

[7] Hudson HM and Larkin RS, "Accelerated image reconstruction using ordered subsets of projection data," *IEEE Trans. Med. Imaging*, vol. 13, pp. 601-609, 1994.

[8] Papoulis A, Probability, Random Variables, and Stochastic Processes, Second Edition, New York, McGraw-Hill, 1984.

[9] Shepp LA and Logan B, "The Fourier reconstruction of a head section," *IEEE Trans. Nuclear Science*, vol. 21, pp. 21-43, 1974.

[10] Tretiak O and Metz CE, "The exponential Radon transform," *SIAM J Appl Math*, vol. 39, pp. 341-354, 1980.

[11] Gordon R, Bender R, and Herman GT, "Algebraic reconstruction techniques (ART) for three dimensional electron microscopy and X-ray photography," *J. Theory Biol.*, vol. 29, pp. 471-481, 1970.

[12] Hart H and Liang Z, "Bayesian Image Processing in Two Dimensions," *IEEE Trans. Medical Imaging*, vol. 6, pp. 201-208, 1987.

[13] Barrett HH, Wilson DW, and Tsui BMW, "Noise properties of the EM algorithm: I. Theory," *Phys. Med. Biol.*, vol. 39, pp. 833-846, 1994.

[14] Wilson DW, Tsui BMW, and Barrett HH, "Noise properties of the EM algorithm: II. Monte Carlo simulations," *Phys. Med. Biol.*, vol. 39, pp. 847-871, 1994.

[15] Fessler JA "Mean and variance of implicitly defined biased estimators (such as penalized maximum likelihood): applications to tomography," *IEEE Trans. Image Processing*, vol. 5, pp. 493-506, 1996.

[16] Wang W and Gindi G, "Noise analysis of MAP-EM algorithms for emission tomography," *Phys. Med. Biol.*, vol. 42, pp. 2215-2232, 1997.

[17] Qi J and Leahy RM, "Resolution and noise properties of MAP reconstruction for fully 3D PET," *IEEE Trans. Med. Imaging*, vol. 19, pp. 493-506, 2000.

[18] Kunyansky LA, "A new SPECT reconstruction algorithm based on the Novikov explicit inversion formula," *Inverse Problems*, vol. 17, pp. 293-306, 2001.

[19] Lious AK, "Orthogonal function series expansions and the null space of the Radon transform," *SIAM J Math. Anal*. vol. 15, pp. 621-633, 1984.

[20] Natterer F, *The Mathematics of Computerized Tomography*, Wiley-Teubner, New York, 1986.

[21] Aguilar V, Ehrenpreis L, and Kuchment P, "Range conditions for the exponential Radon transform," *J. d'Analyse Mathematique*, vol. 68, pp. 1-13, 1996.

[22] Aguilar V and Kuchment P, "Range conditions for the multidimensional exponential X-ray transform," *Inverse Problems*, vol. 11, pp, 977-982, 1995.

[23] Öktem O, "Extension of separately analytic functions and applications to range characterization of the exponential Radon transform," (in Complex Analysis and Applications, Warsaw, 1997), *Ann. Polon. Math*. vol. 70, pp. 195-213, 1998.

[24] Ponomarev I, "Correction of emission tomography data: effects of detector displacement and non-constant sensitivity," *Inverse Problems*, vol. 10, pp. 1-8, 1995.

[25] Natterer F, "Range condition in tomography," Technical Note, July, 1999. (http://wwwmath1.uni-muenster.de/num/Preprints/2004/ natterer_ 2).

[26] Anastasio MA, Pan X, and Clarkson E, "Comments on the filtered backprojection algorithms, range conditions, and the pseudoinverse solution," *IEEE Trans. Medical Imaging*, vol. 20, pp. 539-542, 2001.

[27] Press WH, Teukolsy SA, Vetterling WT, and Flannery BP, *Numerical Recipes in C*, Cambridge University Press, 1992.

[28] Dibella E, Barclay A, Eisner R, and Schaefer R, "A comparison of rotation-based methods for iterative reconstruction algorithms," *IEEE Trans. Nucl. Science*, vol. 43, pp. 3370-3376, 1996.

[29] Wallis JW and Miller TR, "An optimal rotator for iterative reconstruction," *IEEE Trans. Med. Imaging*, vol. 16, pp. 118-123, 1997.

[30] You J, Li T, and Liang Z, "A classical FBP implementation of Novikov's inversion formula for quantitative SPECT imaging," *IRIS Lab technical report, SUNY at Stony Brook,* March, 2004.